JOURNAL OF SYNCHROTRON RADIATION

ISSN 1600-5775

Development of an X-ray imaging detector for high-energy X-ray microtomography

Masato Hoshino,* Kentaro Uesugi and Naoto Yagi

Spectroscopy and Imaging Division, Japan Synchrotron Radiation Research Institute, 1-1-1 Kouto, Sayo, Hyogo 679-5198, Japan. *Correspondence e-mail: hoshino@spring8.or.jp

Received 11 October 2019
Accepted 6 April 2020

Edited by Y. Amemiya, University of Tokyo, Japan

Keywords: high-energy X-ray microtomography; X-ray imaging detectors; scintillators; fossils.

A dedicated X-ray imaging detector for 200 keV high-energy X-ray microtomography was developed. The novelty of the detector is a large-format camera lens employed for a wide field of view. Several scintillators were evaluated in terms of the degree of efficiency of detection for high-energy X-ray photons and the modulation transfer function. For tomographic measurement, a high-definition CMOS camera was incorporated in the detector to achieve a high spatial resolution while keeping the field of view wide. Rocks with fossil inclusions were imaged to demonstrate the applicability of the detector to high-energy X-ray microtomography.

1. Introduction

High energy and high spatial resolution (high-resolution) X-ray microtomography has a great potential to promote the non-destructive observation of rocks, fossils, industrial materials, metallic objects and so on (Di Michiel *et al.*, 2005; Tafforeau *et al.*, 2006; Finegan *et al.*, 2016; Cau *et al.*, 2017; Levitt *et al.*, 2017; Uesugi & Hoshino, 2017; Wang *et al.*, 2019). With respect to high-energy measurements, industrial computed tomography systems enable non-destructive observation with high-energy X-rays generated by an X-ray tube with a voltage of several hundred kilovolts (for example, a maximum tube voltage of 450 kV can be found in the TOSCANER-20000 series, https://www.toshiba-itc.com/en/hihakai/toscaner-20000/). However, they are not suitable for high-resolution observations because of the lack of X-ray flux. In comparison, a high-energy synchrotron is a promising X-ray source for high-energy high-resolution X-ray microtomography. The quasi-parallel beam from the source allows us to achieve high-resolution tomography even in the high-energy region. In addition, the partially coherent beam makes it possible to observe samples by using phase contrast such as propagation-based edge enhancement. There are several synchrotron radiation facilities which can be used for high-energy X-ray imaging at higher than 100 keV (Di Michiel *et al.*, 2005; Ruiz-Yaniz *et al.*, 2015; Cau *et al.*, 2017; Levitt *et al.*, 2017; Wang *et al.*, 2019). In the case of X-ray micro-imaging, especially in the high-energy region, the flux of the beam rather than the monochromaticity becomes an important factor in achieving high-resolution measurements. To address this, the use of a white beam (a polychromatic X-ray beam) would be a unique solution. In our previous study, a white beam from a bending magnet at SPring-8 (Hyogo, Japan) was simply filtered with heavy metals to extract a high-energy X-ray spectrum with a peak energy of 200 keV to observe the metallic cultural heritage (Hoshino *et al.*, 2017). To extend the

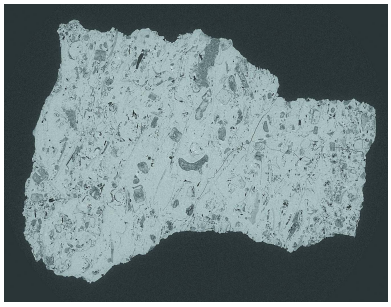

applications of high-energy X-ray microtomography to fossils and metallic objects, improvements to the system, especially through the addition of an X-ray imaging detector, were required for high efficiency in detecting high-energy X-rays and the flexibility to change the spatial resolution and field of view (FOV) in accordance with the sample.

In this study, a dedicated X-ray imaging detector for 200 keV high-energy X-ray microtomography was developed. As a basic concept of this detector, allowing wide-FOV measurements was primarily considered. This is because large objects filled with dense materials such as rocks containing fossils could be the primary application in high-energy and high-resolution X-ray microtomography. Moreover, since the X-ray beam from a bending magnet is spread in the horizontal direction even in the high-energy region, it is basically suitable for tomographic observation of a large object. From these points of view, an X-ray imaging detector which is capable of large-area imaging is essential for synchrotron radiation-based high-energy X-ray microtomography. In addition, the introduction of a high-definition detector serves to keep the FOV wide even in high-resolution imaging, which can be defined by the effective pixel size of the detector. A combination of these factors will realize high-energy and high-resolution X-ray microtomography while keeping the FOV wide.

2. High-energy X-ray microtomography using a white beam

In the case of X-ray imaging carried out to measure the transmission information of a sample, a highly monochromated X-ray beam is not always required. In such a case, a polychromatic X-ray beam called a white or pink beam can be beneficial for high-resolution imaging. A synchrotron radiation-based polychromatic beam can also be used for high-speed measurement (Lame *et al.*, 2003; Di Michiel *et al.*, 2005; Mokso *et al.*, 2011; Shuai *et al.*, 2016; Yashiro *et al.*, 2017; Vegso *et al.*, 2019). In particular, the plentiful flux in the polychromatic beam becomes more important in the high-energy region where the X-ray flux in synchrotron radiation rapidly decreases. With respect to high-energy and high-resolution X-ray imaging, a high-energy synchrotron radiation facility such as SPring-8 is suitable. Although the critical energy in the white beam from the bending magnet at SPring-8 is 28.9 keV, X-rays with much higher energies are also included in the spectrum. Bending magnet beamline BL28B2 is one of the few beamlines which have access to the white beam at SPring-8 (Chikaura *et al.*, 2001). The simplest technique for extracting polychromatic high-energy X-rays is to use an appropriate absorber. A high-energy X-ray spectrum with a peak energy of ∼200 keV can be obtained by using an absorber composed of a tungsten plate with a thickness of 0.5 mm and a lead plate with a thickness of 2 mm. The calculated spectrum can be seen elsewhere (Hoshino *et al.*, 2017). To eliminate speckles from the absorber itself, the absorber is rotated with a rotational speed of 1500–2000 revolutions per minute. The distance from the absorber to a sample is ∼5 m. Through all measurements and observations in this study, the 200 keV high-energy spectrum was used. The sample stage for tomography has a standard configuration composed of a high-precision rotational stage (SPU-1F; Kohzu Precision), orthogonal swivel stages to adjust tilts of the rotational axis, and horizontal and vertical translation stages. The vertical translation stage is capable of scanning a long sample with a motion range of ±300 mm. An X-ray imaging detector can be installed at another downstream experimental hutch. There is a shielding wall except around the optical axis of the X-ray beam between the two experimental hutches that prevents high-energy scattered X-rays from entering into the electrical device of the detector directly. The X-ray imaging detector is set on a detector stage composed of horizontal and vertical stages, and a swivel stage for adjusting the vertical pixel line to be parallel to the vertical translation of a sample.

3. X-ray imaging detector for high-energy X-ray microtomography

When designing the X-ray imaging detector for high-energy X-ray microtomography, a lens-coupled visible-light conversion-type system was employed to allow for the flexibility to change the pixel size and FOV (Koch, 1994; Uesugi *et al.*, 2011; Mittone *et al.*, 2017). In particular, a tandem-lens system used between the scintillator and camera enables us to easily change the effective pixel size by replacing the lenses. In this study, a large-format camera lens (Planar 135/3.5; Carl Zeiss) for a large-format camera was used as the first lens to enable a large area to be imaged without vignetting. The focal length (f) and F number (F) are f = 135 mm and F = 3.5, respectively. With this type of lens, the distance from the scintillator to the lens, called the flange focal length, is almost equal to f. A photograph of the X-ray detector developed is shown in Fig. 1. This system employs an 'L-shaped' configuration to protect the camera from the direct incidence of high-energy X-rays transmitted through the scintillator. In addition, X-ray scattering from the prism mirror can be effectively reduced by configuring the optical axis of the lenses to be normal to that

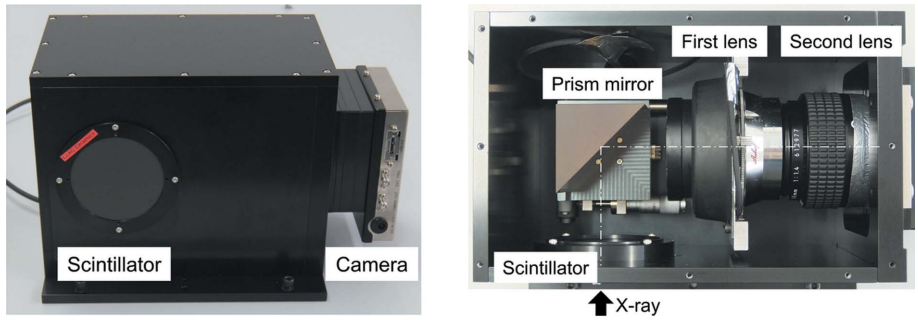

Figure 1
The developed X-ray imaging detector. (*a*) Exterior and (*b*) top view of the interior.

of X-rays in a horizontal plane because incident X-rays from the bending magnet are horizontally polarized. In the photograph shown in Fig. 1, the second lens, which has a focal length of 35 mm (AI Nikkor 35 mm *f*/1.4 S; Nikon), is set close to the first lens. The first lens is movable along the optical axis by a linear actuator to adjust the focus. As an imaging device, a high-definition industrial CMOS camera, C13949-50U [4096 (H) × 3008 (V) pixels, 3.45 µm pixel^{-1}, dynamic range of 4565:1, full-well capacity of 10 500 e$^-$, USB3.0 interface; Hamamatsu Photonics], was used to achieve a wide FOV with a smaller pixel size.

3.1. Evaluation of X-ray scintillators

In high-energy X-ray imaging, considering the conversion efficiency (the average number of electrons in the sensor created by each incident X-ray photon via a scintillator and a visible-light optical system) while keeping the image quality good is important. Here, several scintillators were evaluated in terms of the efficiency and modulation transfer function (MTF) of images to determine the optimal scintillator for high-energy X-ray microtomography carried out using the developed detector. A list of the scintillating materials and thicknesses that were under evaluation is shown in Table 1. There were three types of scintillating materials. The first was a $Lu_3Al_5O_{12}$:Ce^+ (LuAG:Ce^+) single-crystal scintillator. The second was a LuAG:Ce^+ ceramic scintillator. LuAG was selected as the scintillating material because the wavelength of the maximum emission matched well with the spectral sensitivity of the high-definition CMOS camera shown above. Moreover, the ceramic scintillator was used so as to compare its performance with the single-crystal one. The third was a Gd_2O_2S:Tb^+ (GADOX or P43) powder scintillator which has been used as a standard scintillating material at SPring-8. The basic properties of these scintillating materials can be found elsewhere (Martin & Koch, 2006; Nikl *et al.*, 2007; Kameshima *et al.*, 2019). When evaluating the efficiency and the MTF, only the scintillator was replaced. The effective pixel size of the detector was 12.98 µm pixel^{-1}. For evaluating the efficiency, intensity profiles along the vertical direction of the beam at the detector position were measured. Although the absolute efficiency (conversion efficiency) was not measured, the relative intensity profiles represent the relative efficiency of the detector as a variable of the scintillator. Normalized intensity profiles are shown in Fig. 2(*a*). In the actual measurements, each scintillator was evaluated with different exposure times. Since the digitalized signal generated on the camera had an adequate linearity under different exposure times, intensity profiles were corrected so that they could be compared relatively. As shown in Fig. 2(*a*), a LuAG single-crystal scintillator of 2000 µm thickness provided the highest efficiency for the 200 keV beam. In comparison, the efficiency of a P43 scintillator of 25 µm in thickness was less than 10% of that of the LuAG of 2000 µm in thickness. Although thick scintillators provide higher efficiency because of their relatively high ability to stop high-energy X-rays, the image quality, represented by the MTF, has to also be considered for actual use. To evaluate the MTF, a test chart which had line and space patterns (Type-14 test chart; Moriyama X-ray Equipments Co. Ltd, Japan) was used. The test chart was made of lead with a pattern thickness of 30 µm. To calculate the MTF, the reference contrast was estimated from the transmittance of lead at the uniform region by using 25 µm-thick P43 scintillator. MTFs measured with the

Table 1
A list of scintillating materials and thicknesses used for evaluating efficiency and the MTF.

	Material	Type	Thickness (µm)
No. 1	$Lu_3Al_5O_{12}$:Ce^+	Single crystal	500
No. 2	$Lu_3Al_5O_{12}$:Ce^+	Single crystal	1000
No. 3	$Lu_3Al_5O_{12}$:Ce^+	Single crystal	2000
No. 4	$Lu_3Al_5O_{12}$:Ce^+	Ceramics	500
No. 5	Gd_2O_2S:Tb^+	Powder	25
No. 6	Gd_2O_2S:Tb^+	Powder	50

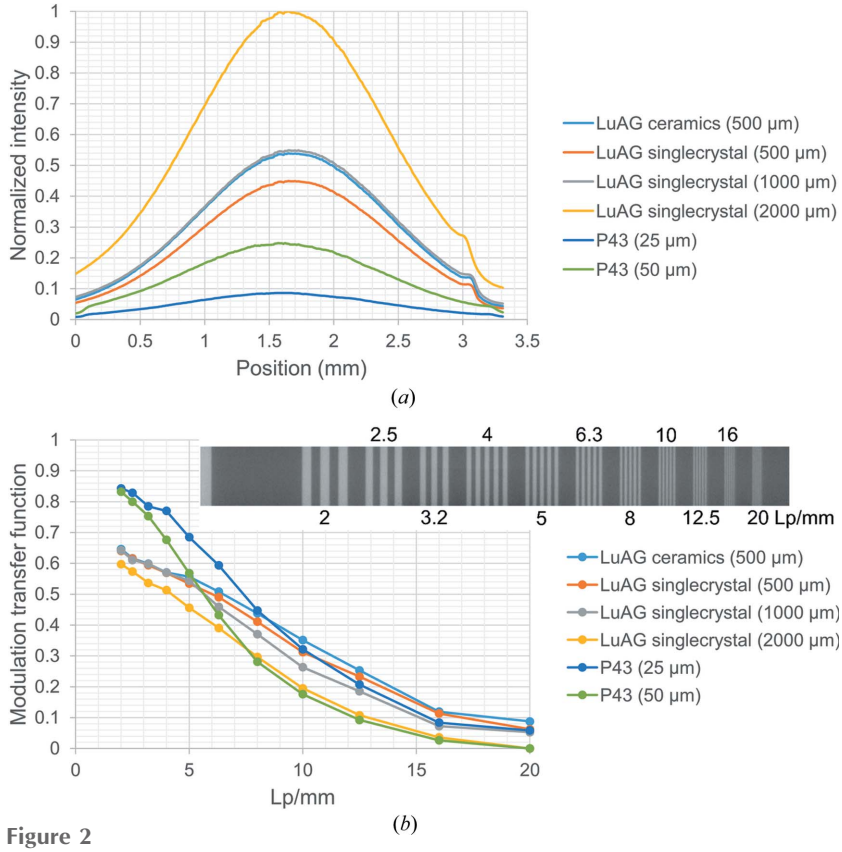

Figure 2
(*a*) Normalized intensity profiles along the vertical direction of the 200 keV white beam and (*b*) MTFs measured with different scintillators. The inset is the transmission image of the test chart observed with the LuAG ceramic scintillator of 500 µm in thickness.

different scintillators listed in Table 1 are shown in Fig. 2(*b*). The inset is an example of a transmission image of the test chart obtained with the LuAG ceramic scintillator. As a result, the thin P43 scintillator showed the best image contrast in the lower-frequency region. Regarding the LuAG single crystals, the MTF worsened while the efficiency improved as the thickness increased. LuAG ceramic and single crystal of 500 µm thickness showed similar MTFs, while the ceramic showed slightly higher efficiency. In addition, 500 µm-thick LuAG scintillators (both ceramic and single crystal) and the 25 µm-thick P43 scintillator showed similar properties in the frequency region higher than 8 line-pairs mm^{-1}. When considering both highly efficient imaging and MTFs, LuAG ceramic or single-crystal scintillators of 500 µm in thickness are good candidates for 200 keV high-energy X-ray microtomography with a pixel size of 12.98 µm. These results also suggest that thick LuAG scintillators have the potential to make high-speed observation possible with a short exposure time while image quality (spatial resolution and contrast) worsens. On the contrary, a thinner scintillator would provide better image quality at the expense of measurement speed.

4. Demonstration of high-energy X-ray microtomography with a wide field of view

As a demonstration of high-energy X-ray microtomography using the developed X-ray detector, an elliptical nodule was measured. Usually, a fossil may be embedded in such a nodule. A photograph of the nodule is shown in Fig. 3(*a*). The propagation distance from the sample to the detector was set to 3 m in this measurement. Then, the effective pixel size at the sample position was 12.15 µm, which was slightly smaller than the pixel size shown above. This is because the projection image was slightly magnified by the long propagation distance. Therefore, the horizontal FOV in the image was calculated to be 49.8 mm. Regarding the conditions for measuring the nodule, the number of projections was 7200 and the exposure time was 25 ms. A LuAG ceramic scintillator of 500 µm in thickness was chosen for this measurement. Approximately 4 min was required to obtain all the projection images for a single tomographic scan. Since the effective beam size along the vertical direction in the 200 keV region was ∼1.5 mm at 45 m from the source [see Fig. 2(*a*)], the nodule was scanned along the vertical direction at 1.42 mm per step. Thirty tomographic scans were required for measuring the whole shape of the nodule. Cross-sectional images in different orthogonal directions are shown in Figs. 3(*b*)–3(*d*). To improve the signal-to-noise ratio in the images, a three-dimensional (3D) Gaussian filter ($\sigma x = 1$, $\sigma y = 1$ and $\sigma z = 1$) of the *ImageJ* (https://imagej.nih.gov/ij/) plugin was applied. The inside of the nodule could be clearly observed. In particular, the fossil of a shell could be found at the centre of the nodule. A 3D view of the shell obtained by inverting the image contrast is shown in Fig. 3(*e*). *Drishti*, a multi-platform open-source volume-rendering software for the 3D visualization of tomographic data, was used for rendering in this case (Limaye, 2012). A complex structure in the nodule as well as the fossil inclusion could be clearly observed with the developed X-ray imaging detector.

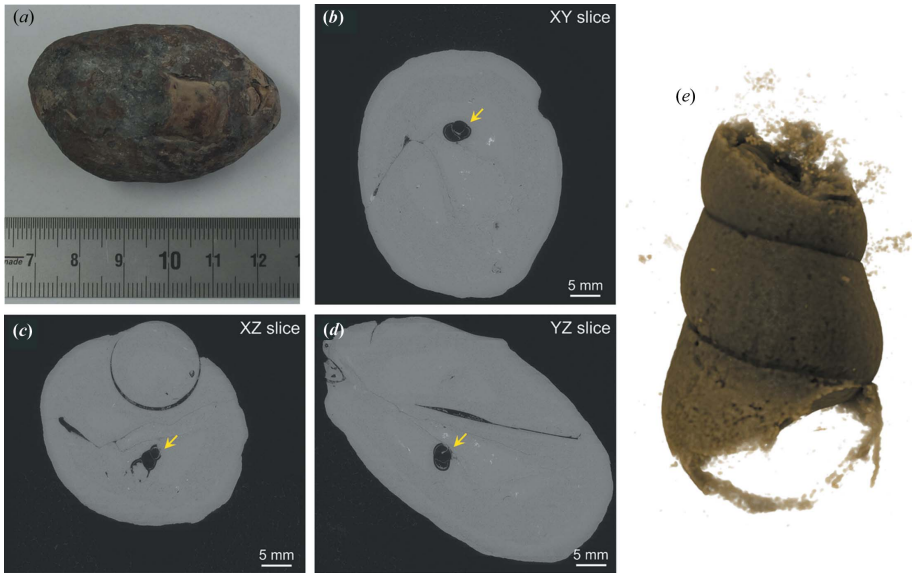

Figure 3
(*a*) Nodule. Cross-sectional images of the nodule in the (*b*) *XY*, (*c*) *XZ* and (*d*) *YZ* directions. (*e*) Three-dimensional view of a shell (indicated by arrows) embedded in the nodule.

5. Application to high-energy and high-resolution X-ray microtomography

As a merit of using the tandem-lens system, the effective pixel size and, consequently, the effective FOV can be easily changed by replacing the second lens. Here, the second lens was replaced with a camera lens with a focal length of 105 mm (AF-S NIKKOR 105 mm *f*/1.4 E ED; Nikon). This meant that the effective pixel size became smaller because the magnification factor in the tandem-lens system defined by the ratio of the focal lengths became larger. Another high-definition CMOS camera, VCXU-201M.R [5472 (H) × 3648 (V) pixels, 2.4 µm $pixel^{-1}$, dynamic range of 3548:1, USB3.0 interface; Baumer GmbH], was used. The effective pixel size of the X-ray imaging detector was 3.13 µm $pixel^{-1}$. In the following measurements, a LuAG ceramic scintillator of thickness 500 µm was used. To demonstrate the effect of a smaller pixel size, the MTF was measured with the same test chart shown in Fig. 2(*b*). The MTF obtained with a pixel size of 3.13 µm $pixel^{-1}$ is shown in Fig. 4. For comparison only, the result obtained with a pixel size of 12.98 µm $pixel^{-1}$ is also shown. Although the only difference in this comparison is the effective pixel size, the smaller pixel size

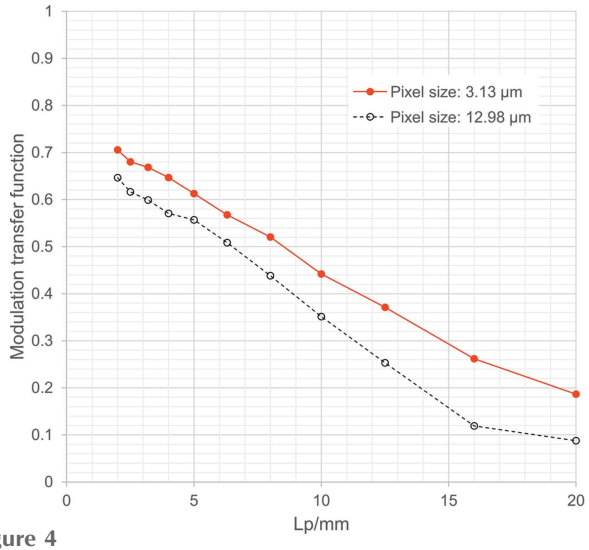

Figure 4
The MTF measured with an effective pixel size of 3.13 µm. For comparison, the MTF measured with a pixel size of 12.98 µm is also shown.

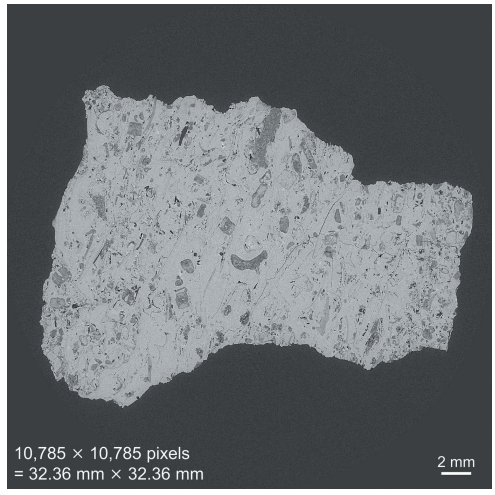

Figure 5
A cross-sectional image of limestone obtained by high-energy and high-definition X-ray microtomography. The effective pixel size is 3.0 µm pixel^{-1}.

contributed to improving the image quality even in the 200 keV region. As a demonstration of high-energy and high-resolution X-ray microtomography, a piece of limestone containing small fossils was observed as a natural test chart. This time, the propagation distance from the sample to the detector was set to 2 m. The effective pixel size at the sample position was 3.0 µm pixel^{-1}. Then, the effective horizontal FOV corresponded to 16.4 mm. Here, an offset scanning method was employed to extend the effective horizontal FOV. The amount of shift of the rotational axis from the centre of the projection image was 8 mm. Regarding the conditions for measuring the limestone, the number of projections was 7200 and the exposure time was 120 ms. Approximately 40 min was required to obtain all the projection images. A cross-sectional image of the limestone is shown in Fig. 5. As was the case with the cross-sectional images shown in Fig. 3, the 3D Gaussian filter ($\sigma x = 1$, $\sigma y = 1$ and $\sigma z = 1$) was applied. A lot of small fossils such as foraminifera were clearly visualized in lower-density regions. In this imaging, the cross-sectional image was composed of more than 1×10^8 pixels. The high-definition high-energy X-ray microtomography was capable of measuring a sample which had a diameter of several tens of millimetres with a voxel size of a few micrometres.

One of the merits of using 200 keV high-energy X-rays is the outstanding penetration power. For instance, more than 10% transmission can be expected for iron with a thickness of 20 mm when using a 200 keV beam. This means that non-destructive and high-resolution inspection of the contents of a metallic container can also be a potential application of high-energy X-ray microtomography. As a feasibility study on visualizing an object in a metallic container, a piece of limestone set in a stainless-steel pipe (SUS304) was imaged. The thickness of the pipe wall was ~2 mm. For this measurement, the effective pixel size at the sample position was set to 5.09 µm pixel^{-1} by using a second lens with a focal length of 85 mm (AF-S NIKKOR 85 mm *f*/1.4 G; Nikon). The CMOS camera used was a C13949-50U. The propagation distance was set to 3 m. Since the diameter of the pipe was larger than the effective FOV of the detector, the offset scanning method was used. Regarding the experimental conditions, the number of projections was 7200, the exposure time was 40 ms and the amount of offset was 5 mm. A cross-sectional image of the sample is shown in Fig. 6(*a*). The 3D Gaussian filter ($\sigma x = 1$, $\sigma y = 1$ and $\sigma z = 1$) was also applied and the limestone in the pipe was successfully visualized. A magnified image of the square region is shown in Fig. 6(*b*). A small fossil with eight spokes can be clearly observed even in the metallic container. Thus, the use of 200 keV high-energy X-rays has a great advantage for measuring a sample under special atmospheric conditions in a sealed container.

6. Discussion

In the demonstration of high-energy X-ray microtomography, rocks with fossil inclusions such as a nodule and a piece of limestone were successfully imaged with the lens-coupled X-ray imaging detector developed in this study. As the first lens in the tandem-lens system, a large-format camera lens with $F = 3.5$ was employed. Basically, the large numerical aperture of the lens, which corresponds to a smaller value of F, is helpful for realizing a strong ability to collect light and high-resolution measurements. The large numerical aperture (NA) also means a small depth of focus. The depth of focus of the lens z can be described by the equation

$$z = \pm \frac{\lambda}{2\mathrm{NA}^2} \simeq \pm 2\lambda F^2, \qquad (1)$$

where λ is the wavelength and NA is the numerical aperture. The depth of focus of the lens with $F = 3.5$ is calculated to be 25.5 µm (= $2|z|$), where λ is set at 520 nm, which is the peak wavelength of LuAG luminescence. In the actual observation, however, the effective pixel size should be considered in the

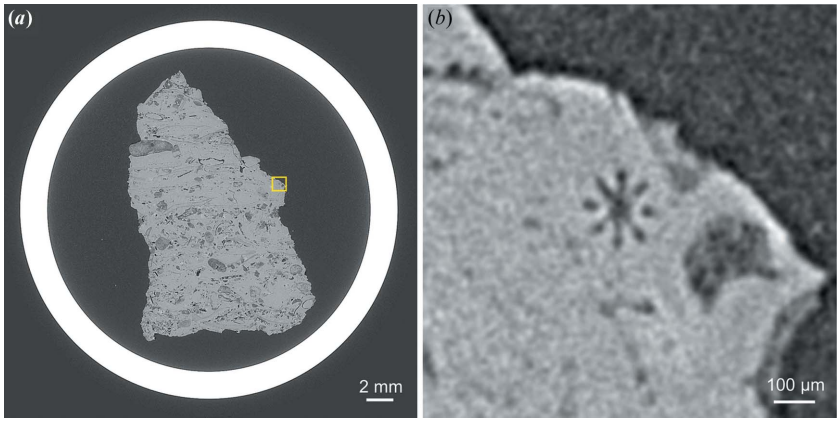

Figure 6
(*a*) A cross-sectional image of limestone set in stainless-steel (SUS304) pipe with a wall thickness of 2 mm. (*b*) A magnified image at the square shown in (*a*).

discussion of the depth of focus. A theoretical spatial resolution of the lens is given by

$$\delta = 0.61\frac{\lambda}{\mathrm{NA}} \simeq 1.22\lambda F. \quad (2)$$

The theoretical resolution of the lens with $F = 3.5$ is calculated to be 2.22 µm, which is smaller than the effective pixel size in this study. To discuss the effective depth of focus in the detector with the pixel size larger than δ, an additional term should be added in equation (1). From the relation between the spatial resolution and the numerical aperture, the effective numerical aperture with a pixel size of d is assumed to be $\mathrm{NA}' = \mathrm{NA} \times \delta/d$. Then, the effective depth of focus z' can be modified as follows,

$$z' = z \times \left(\frac{d}{\delta}\right)^2. \quad (3)$$

When the effective pixel size is 12.15 µm for the wide FOV imaging, the effective depth of focus is estimated to be 764 µm. This is larger than the thickness of the scintillator used in tomographic observations. In comparison, the effective depth of focus is estimated to be 46.6 µm at the pixel size of 3.0 µm, which is the smallest pixel size in this study. In this situation, the scintillator is thicker than the effective depth of focus. In addition, transmission of the 200 keV beam for the 500 µm-thick LuAG is ~85% from the NIST database (Hubbell & Seltzer, 2004). This means that luminescence can be expected from the entire region along the X-ray beam path in the scintillator. Consequently, blurred signals generated in out-of-focus regions and stray light might affect the projection images. However, the MTF measured with the smaller pixel size still provided a better property compared with that measured with the large pixel size, as shown in Fig. 4. Further optimization for the thickness of the scintillator will be required for high-energy and high-resolution X-ray microtomography with the effective pixel size smaller than several micrometres.

On the other hand, a thicker scintillator, which is potentially thicker than the effective depth of focus, has the possibility of acquiring images with shorter exposure times at the expense of image quality, as shown in Fig. 2. A shorter exposure time is preferred in high-throughput and fast measurements. Since the vertical beam size of the 200 keV X-ray from the bending-magnet source is narrow, as shown in Fig. 2(*a*), fast acquisition of images is required for multiple tomographic scans to observe the entire region of a large object.

When considering phase-contrast imaging for enhancing the image contrast with synchrotron radiation, the propagation distance is an important parameter. Weitkamp *et al.* presented a critical propagation distance by using a given pixel size (d) and X-ray energy (wavelength λ), $l_c = (2d)^2/\lambda$ (Weitkamp *et al.*, 2011). The propagation distance l should be shorter than l_c to fulfil the near-field condition. This is a function of X-ray photon energy. Therefore, a long propagation distance would basically be expected for high-energy X-ray imaging with phase contrast. In this study, the propagation distance was 3 m at a pixel size of 12.15 µm. At this pixel size, l_c is calculated to be 95 m when the X-ray energy is 200 keV. Therefore, the propagation distance should be much longer to utilize the phase contrast more effectively at d = 12.15 µm. For high-resolution imaging, l_c is calculated to be 5.8 m (d = 3.0 µm). Since the actual propagation distance was 2 m, a little edge-enhancement effect caused by X-ray refraction could be observed at the boundary of the limestone shown in Fig. 5. Under the current experimental conditions, however, the maximum propagation distance was limited by the length of the experimental hutch. To utilize the phase contrast more effectively, observation of local fine structures in large fossils and rocks with a higher spatial resolution might be interesting. When the effective pixel size is set to 1 µm or sub-µm, l_c will be shorter than 645 mm, even in the 200 keV region, which is easily arranged on an experimental bench.

Some browning on the first lens was seen after several days of use as a result of high-energy X-rays scattered from the prism mirror, although the optical axis of the visible-light optics was set normal to that of the X-rays in the horizontal plane. The browning of the lens degraded the transmission of visible light. Fortunately, this browning can be removed by irradiation with a commercial desk lamp. The browning effect may be reduced by setting radiation-resistant glass between the prism mirror and the first lens. In addition, fundamentally reducing scattering should also be considered. In this study, a massive prism mirror was used to make the configuration as simple as possible. By replacing the mirror with a thin one, X-rays scattered from the mirror might be reduced.

7. Conclusions

The performance of high-energy X-ray microtomography in an energy region around 200 keV was improved by developing a dedicated X-ray imaging detector. The lens of the large-

format camera in the detector could cover a horizontal FOV up to 50 mm. Employing such a lens is a simple technique for realizing large-area imaging with lens-coupled visible-light conversion-type X-ray imaging detectors. The effective horizontal FOV will be expanded to ∼100 mm by employing an offset scanning method. This is a promising technique for measuring, for instance, fossils embedded in large-sized rocks. Also, high-resolution tomographic measurement with an effective pixel size of a few micrometres was demonstrated. This can be an outstanding feature of synchrotron radiation-based high-energy X-ray microtomography.

Acknowledgements

The authors would like to thank Mr Tomoki Fukui for his technical support. This work was carried out with the approval of the SPring-8 Program Review Committee (2017A1373, 2017B1323, 2018A1270, 2018A1464, 2018B1344. 2018B1346, 2019A2018, 2019A1338)

References

Cau, A., Beyrand, V., Voeten, D. F. A. E., Fernandez, V., Tafforeau, P., Stein, K., Barsbold, R., Tsogtbaatar, K., Currie, P. J. & Godefroit, P. (2017). *Nature*, **552**, 395–399.

Chikaura, Y., Iida, S., Kawado, S., Mizuno, K., Kimura, S., Matsui, J., Umeno, M., Ozaki, T., Shimura, T., Suzuki, Y., Izumi, K., Kawasaki, K., Kajiwara, K. & Ishikawa, T. (2001). *J. Phys. D Appl. Phys.* **34**, A158–A162.

Di Michiel, M., Merino, J. M., Fernandez-Carreiras, D., Buslaps, T., Honkimäki, V., Falus, P., Martins, T. & Svensson, O. (2005). *Rev. Sci. Instrum.* **76**, 043702.

Finegan, D. P., Tudisco, E., Scheel, M., Robinson, J. B., Taiwo, O. O., Eastwood, D. S., Lee, P. D., Di Michiel, M., Bay, B., Hall, S. A., Hinds, G., Brett, D. J. L. & Shearing, P. R. (2016). *Adv. Sci.* **3**, 1500332.

Hoshino, M., Uesugi, K., Shikaku, R. & Yagi, N. (2017). *AIP Adv.* **7**, 105122.

Hubbell, J. H. & Seltzer, S. M. (2004). *Tables of X-ray Mass Attenuation Coefficients and Mass Energy-Absorption Coefficients from 1 keV to 20 MeV for Elements Z = 1 to 92 and 48 Additional Substances of Dosimetric Interest*. Report NISTIR 5632. National Institute of Standards and Technology, Gaithersburg, MD, USA.

Kameshima, T., Takeuchi, A., Uesugi, K., Kudo, T., Kohmura, Y., Tamasaku, K., Muramatsu, K., Yanagitani, T., Yabashi, M. & Hatsui, T. (2019). *Opt. Lett.* **44**, 1403–1406.

Koch, A. (1994). *Nucl. Instrum. Methods Phys. Res. A*, **348**, 654–658.

Lame, O., Bellet, D., Michiel, M. D. & Bouvard, D. (2003). *Nucl. Instrum. Methods Phys. Res. B*, **200**, 287–294.

Levitt, M. R., Barbour, M. C., du Roscoat, S. R., Geindreau, C., Chivukula, V. K., McGah, P. M., Nerva, J. D., Morton, R. P., Kim, L. J. & Aliseda, A. (2017). *J. Neurointerv. Surg.* **9**, doi:10.1136/neurintsurg-2016-012479.

Limaye, A. (2012). *Proc. SPIE*, **8506**, 85060X.

Martin, T. & Koch, A. (2006). *J. Synchrotron Rad.* **13**, 180–194.

Mittone, A., Manakov, I., Broche, L., Jarnias, C., Coan, P. & Bravin, A. (2017). *J. Synchrotron Rad.* **24**, 1226–1236.

Mokso, R., Marone, F., Haberthür, D., Schittny, J. C., Mikuljan, G., Isenegger, A., Stampanoni, M., McNulty, I., Eyberger, C. & Lai, B. (2011). *AIP Conf. Proc.* **1365**, 38–41.

Nikl, M., Mares, J. A., Solovieva, N., Li, H.-L., Liu, X.-J., Huang, L.-P., Fontana, I., Fasoli, M., Vedda, A. & D'Ambrosio, C. (2007). *J. Appl. Phys.* **101**, 033515.

Ruiz-Yaniz, M., Koch, F., Zanette, I., Rack, A., Meyer, P., Kunka, D., Hipp, A., Mohr, J. & Pfeiffer, F. (2015). *Appl. Phys. Lett.* **106**, 151105.

Shuai, S., Guo, E., Phillion, A. B., Callaghan, M. D., Jing, T. & Lee, P. D. (2016). *Acta Mater.* **118**, 260–269.

Tafforeau, P., Boistel, R., Boller, E., Bravin, A., Brunet, M., Chaimanee, Y., Cloetens, P., Feist, M., Hoszowska, J., Jaeger, J.-J., Kay, R. F., Lazzari, V., Marivaux, L., Nel, A., Nemoz, C., Thibault, X., Vignaud, P. & Zabler, S. (2006). *Appl. Phys. A*, **83**, 195–202.

Uesugi, K. & Hoshino, M. (2017). *Proc. SPIE*, **10391**, 103911D.

Uesugi, K., Hoshino, M. & Yagi, N. (2011). *J. Synchrotron Rad.* **18**, 217–223.

Vegso, K., Wu, Y., Takano, H., Hoshino, M. & Momose, A. (2019). *Sci. Rep.* **9**, 7404.

Wang, H., Atwood, R. C., Pankhurst, M. J., Kashyap, Y., Cai, B., Zhou, T., Lee, P. D., Drakopoulos, M. & Sawhney, K. (2019). *Sci. Rep.* **9**, 8913.

Weitkamp, T., Haas, D., Wegrzynek, D. & Rack, A. (2011). *J. Synchrotron Rad.* **18**, 617–629.

Yashiro, W., Noda, D. & Kajiwara, K. (2017). *Appl. Phys. Expr.* **10**, 052501.